UCLA

Title

MEMS gyro drift compensation using multiple rate measurements derived from a single resonator

Permalink

ISBN

Authors

Ge, Howard H
Behbahani, Amir H
M'Closkey, Robert T

Publication Date

2018

Peer reviewed

MEMS gyro drift compensation using multiple rate measurements derived from a single resonator

Howard H. Ge, Robert M'Closkey†

Mechanical and Aerospace Engineering

Samueli School of Engineering and Applied Science

University of California, Los Angeles, CA 90095

Abstract

Axisymmetric resonators possess multiple pairs of nominally degenerate modes, each of which can be configured as a Corilois vibratory gyro. In this paper we report a technique to extract simultaneous angular rate measurements from the same resonator. Specifically, both of the $n = 2$ and $n = 3$ pairs of modes in a disk resonator are configured to yield measurements of angular rate. Although the short-term noise is uncorrelated between these rate measurements, the long-term drifts show very strong correlation. A technique is implemented to fuse the two measurements into a single estimate of rate with much lower drift thereby providing a technique for in-situ bias drift compensation.

Index Terms

Gyroscopes, MEMS, inertial sensors, bias self-calibration, gyroscope

I. INTRODUCTION

Coriolis vibratory gyroscopes (CVG) are often considered the most critical component in a strap down inertial navigation system. Such sensors measure the angular rate of rotation through the Coriolis coupling, or exchange of angular momentum, between a pair of resonant modes with nearly equal frequencies. Axisymmetric resonant structures have long been exploited to achieve some of the best performance a CVG can offer. For instance Delco's Hemispherical Gyro is capable of reaching strategic grade performance, while some of the more recent 2D and 3D MEMS implementations promise to enable lost-cost fabrication of such high performance devices [1–5].

An often overlooked advantage offered by axisymmetric resonators is the fact that they possess multiple pairs of nominally degenerate modes. Current state-of-the-art axisymmetric CVGs are all based on exploiting a single mode pair for rate and angle sensing, i.e. either the $n = 2$ pair (the so-called wine glass modes) or the $n = 3$ pair [6–8]. Little research has been devoted to studying the *simultaneous* operation of multiple pairs of modes and to the benefits it may offer. For example, a significant source of long-term drift in MEMS gyros can be attributed to temperature variation of, and thermal gradients within, the resonator. It is not known whether these disturbances affect the higher-order pairs of modes to the same degree as the $n = 2$ pair.

Preliminary results of our study on simultaneously operating both the $n = 2$ and $n = 3$ mode pairs in a single disc resonator are described in detail in [9]. The simultaneously extracted rate measurements show strong correlation between their bias drifts. In this paper, we extend the study of error correlation by examining the effects of external environmental disturbances such as temperature and vacuum pressure drifts.

II. RESONATOR DESCRIPTION AND CONTROL ARCHITECTURE OVERVIEW

The resonator under study is of a planar disc resonator type, which consists of 9 concentric rings coupled together to a central stem by a system of staggered spokes. The outer most ring is 1 cm in diameter and is surrounded by 24 segmented electrodes. The electrodes can be individually configured, or grouped together into a larger electrode, as a drive or a pickoff. A top view of the resonator is shown in Fig. 1. The $n = 2$ and $n = 3$ pairs of mode are the first and second fundamental modes that are nominally isolated from central stem vibration, with Coriolis coupling factors approximately those of a uniform ring resonator (which are 0.4 and 0.3, respectively). The modal shape associated with the $n = 2$ modes is essentially elliptical. Fig. 2 illustrates the exaggerated mode shapes. As shown in Fig. 1, the electrodes are arranged in a way so as to maximize the pickoff signals for both pairs of modes. Furthermore, differential driving and sensing is employed for the $n = 3$ pair to further boost the signal-to-noise ratio. It was determined in [9] that for the same drive voltage, the modal displacement for the $n = 3$ is roughly one tenth that of the $n = 2$ mode.

The nominal frequency of the $n = 2$ mode pair is approximately 13.5 kHz, and for the $n = 3$ mode pair it is approximately 27.5 kHz. The approximate 10 kHz difference in resonant frequencies between the pairs of modes permits the separation of the signals associated with the two pairs using filtering. In this case each pair is operated as an independent CVG. However,

---
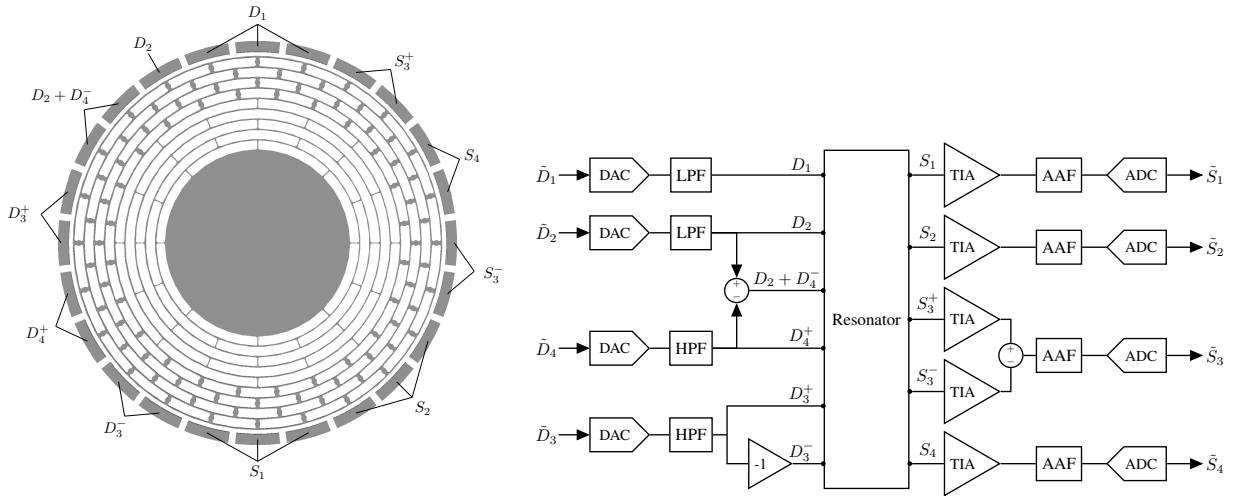
†Corresponding author, rtm@seas.ucla.edu.

Fig. 1. Left: electrode layout and configuration for the resonator. (Right) Functional block diagram showing relationship between electrode pickoff signals and sampled digital signals. Figures from [9].
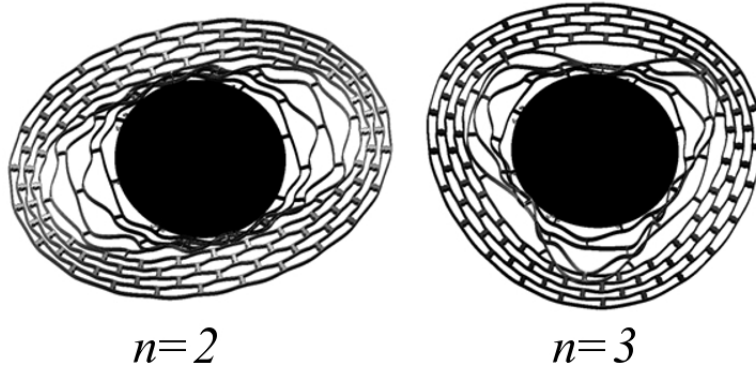

Fig. 2. $n = 2$ and $n = 3$ mode shapes for the UCLA resonator with approximate modal frequencies as follows: $\omega_{n_2} \approx 13.5$ kHz, $\omega_{n_3} \approx 27.5$ kHz.

in order to operate each mode pair as a high-sensitivity CVG, frequency matching must be simultaneously accomplished for both mode pairs. A method was reported in [10] that demonstrated the simultaneous reduction of the frequency mismatch within each pair via mass loading of the resonator. For more details on frequency mismatch and mode matching techniques concerning ring-type resonators, the readers are referred to [11–14]. For the device used in this study, both $n = 2$ and $n = 3$ frequency splits are reduced to about 100 mHz, which is well within the 3 dB bandwidth of the resonance peaks.

The block diagram shown in Fig. 1 illustrates the electrical interface between the resonator and the electronics. All pickoff electrode currents are buffered by trans-impedance amplifiers (TIA) with $10\,\text{M}\Omega$ feedback resistors. A digital signal processor (DSP) executing at an $80\,\text{kHz}$ sample rate interfaces to 16-bit analog-to-digital convertors (ADCs) and digital-to-analog convertors (DACs). The TIA outputs are filtered by anti-alias filters prior to sampling. The anti-alias filters are denoted by the "AAF" blocks in Fig. 1. The block diagram also shows how the electrode signals are consolidated and sampled. The discrete-time signals manipulated by the DSP are given the ~ notation. The automatic gain control (AGC) forcing signals issued by the DSP are denoted $\tilde{D}_1$ and $\tilde{D}_3$ for the $n = 2$ and $n = 3$ pairs, respectively. The FTR forcing signals are denoted $\tilde{D}_2$ and $\tilde{D}_4$ for the $n = 2$ and $n = 3$ pairs, respectively. The signals $\tilde{S}_1$ and $\tilde{S}_3$ are the AGC pick-offs, and $\tilde{S}_2$ and $\tilde{S}_4$ are the force-to-rebalance pick-offs.

Closed-loop operation of the $n = 2$ mode is implemented independent of the $n = 3$ mode pair. The decoupling of the pickoff signals of the two mode pairs is accomplished by utilizing a filter structure similar to that of a lock-in amplifier. Fig. 3 shows the force-to-rebalance (FTR) and the automatic gain control (AGC) loops for controlling the $n = 2$ mode pair. The $n = 3$ control loops are identical in architecture and only differ in the filter and compensator parameters. For succinctness they are not shown in the figure. For each pair of modes, the AGC loop employs a nonlinear amplitude detection followed by a proportional-integral controller. The feedback signal is then amplitude modulated by the resonator output itself with appropriate phase lag added to account for the phase delay in the electronic filters. This implementation offers simplicity, and at the same time can automatically track the gyro frequency drift due to external effects. An alternative (not investigated in this study) is to
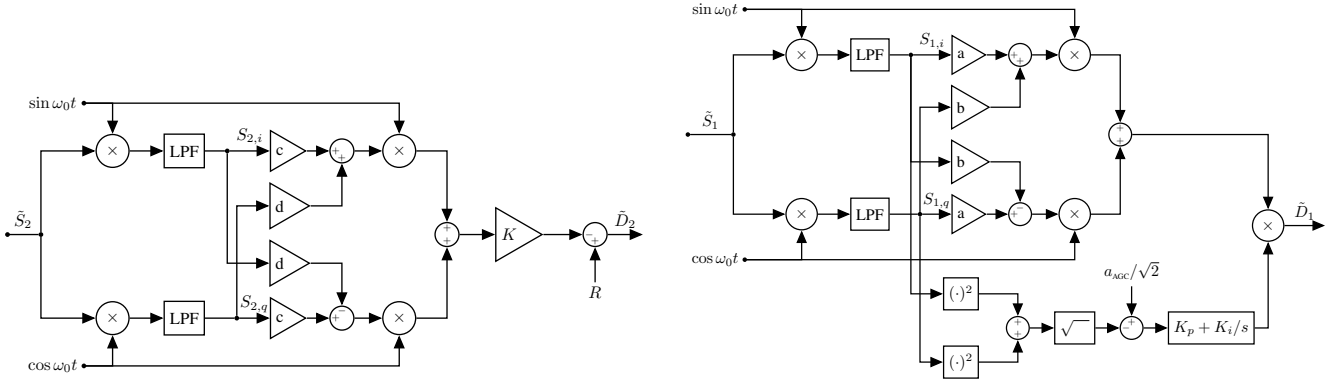
Fig. 3. Left: force-to-rebalance (FTR) controller with lock-in architecture and phase adjustment. Right: automatic gain control (AGC) for sensor excitation. Figures from [9].

employ a phase locked loop. The FTR loop is a simple proportional feedback with a fixed gain, since the goal of FTR loop is to minimize the modal amplitude on the companion mode due to Coriolis coupling, thereby maintaining scale factor linearity.

The angular rate is extracted from the FTR feedback signal by first demodulating with respect to a pair of sine and cosine of the same frequency. The two demodulated signals are then combined to form the magnitude and phase information of the baseband signal. The in-phase component of the signal is the sum of angular rate and bias error. The in-quadrature component is the quadrature error. Further, due to finite phase differences in the analog low-pass filters used for the two loops, a small delta demodulation phase angle needs to be added to the demodulation phase in order to accurately separate rate from quadrature. For details of the loop operations and measurement extraction, the readers are referred to [9].

III. Gyro Characterization and Error Correlation

Since the device under study is not packaged, the tuned resonator is placed inside a vacuum chamber along with the buffer electronics which contains the TIAs. Electrical feedthroughs are provided to allow connections to analog filters and DSP equipment outside the chamber. The chamber is also fitted with a rotary stage to which the gyro is mounted on, so that an angular rotation can be manually applied to test the gyro.

A. Demonstrating simultaneous rate measurement

Simultaneous rate measurements when an angular rotation is applied to the device are shown in Fig. 4. As the figure indicates, the two rate measurements are very consistent and repeatable, albeit with different noise characteristics. A set of zero rate tests in which the gyro operates in an environment with no external rate input other than the earth rotation, were also performed to characterize the key gyro performance indicators under nominal lab conditions. In those tests, the gyro is first operated in the dual mode configuration for two hours, and then switched to n = 2 operation only, and then switched to n = 3 operation only. When operating in single pair, the digital control loop for the other pair simply is turned off. In each of the tests, the electronics and the vacuum pumps were turned on for at least 12 hours prior to the test to avoid any possible extraneous drifts.

The performance parameters are summarized in Table I. The dual mode simultaneous operation has negligible effect on scale factor and bandwidth, however, there is a marginal increase in ARW in both measurements compared to the single pair operation. The ARW increase in the dual mode operation is attributed to nonlinearity in the DAC outputs and is fundamentally unrelated to the motion of the resonator. For this reason, a pair of analog high-pass filters are employed to remove the n = 3 DAC noise power in a neighborhood of the n = 2 modal frequencies, as shown in Fig. 1. Similarly, a pair of low-pass filters are employed to remove the n = 2 DAC noise power in a neighborhood of the n = 3 modal frequencies. The Allan deviation graphs and the noise PSD of the measurements are also shown in Fig. 5. The dash lines in those figures illustrates the dual mode performance. In the plots, Ω_2 denotes the rate measurement associated with the $n = 2$ pair, and Ω_3 that of the $n = 3$ pair.

B. Bias correlation and signal blending

The drifts in rate bias errors of the $n = 2$ mode and the $n = 3$ exhibit strong correlation during simultaneous operation. To demonstrate the correlation, five tests ranging from six hours to over fifteen hours were conducted. To reveal the bias trends, the rate data is filtered by a 10-second moving average filter to remove high frequency noise. The filter window is selected to be approximately equal to the integration time at which the Allan deviation is minimum. All five tests were conducted under nominal laboratory conditions with no temperature control. The filtered signals are denoted $\Omega_{2,lp}$ and $\Omega_{3,lp}$, and are plotted in Fig. 6.
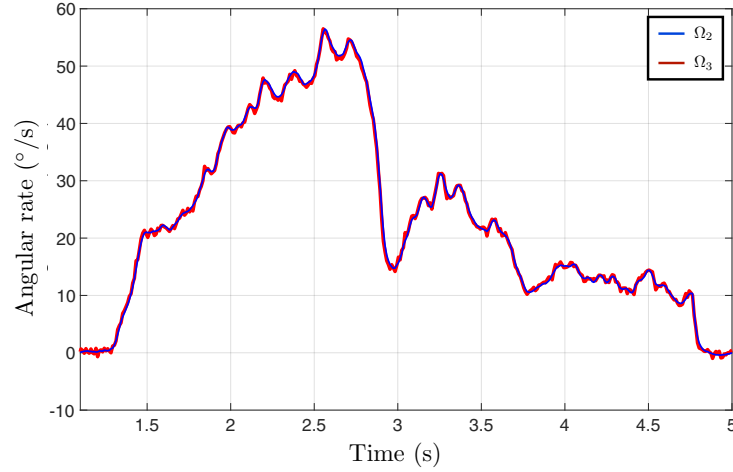
Fig. 4. Simultaneous angular rate measurement with $n = 2$ and $n = 3$ pairs of modes.

TABLE I
DUAL MODE VS. SINGLE MODE GYRO PERFORMANCE COMPARISONS SCALE FACTOR, BANDWIDTH, AND ANGLE RANDOM WALK

Test Case	SF ($^\circ$/s/V)	BW (Hz)	ARW ($^\circ/\sqrt{\mathbf{hr}}$)
$n = 2$ dual	-19.775	10	0.031
$n = 2$ single	-19.734	10	0.025
$n = 3$ dual	62.682	25	0.778
$n = 3$ single	64.629	25	0.517

It is clear that for a given experiment in which both pairs of modes are operated as a CVG, that the Ω_2 and Ω_3 rate biases are strongly correlated. In fact, if the rate signals for the fifteen hour experiment are combined to create the signal $\tilde{\Omega}_{lp} := \lambda \Omega_{2,lp} + (1 - \lambda)\Omega_{3,lp}$, where $\lambda = 0.9192$, then the offset drift of $\tilde{\Omega}_{lp}$ is drastically reduced as shown in Fig. 6. The fact that the long-term drift in the Ω_2 and Ω_3 biases are strongly correlated suggests that it should be possible to combine Ω_2 and Ω_3 into a single rate measurement with lower bias drift. The proposed filter structure for blending the two rate measurements is a set of complementary filters as shown on the left in Fig. 7. This implementation preserves the overall scale factor at all frequencies and offers the advantage of cancelling the correlated bias drift at low frequencies, while optimally blending the two measurements at high frequencies based on the noise spectral densities associated with each measurement, thus enhancing the signal to noise ratio at high frequencies. The readers may find more details regarding the design of this filter structure in [9].

The Allan deviations of the fused rate measurements for the five experiments in Fig. 6 are shown in Fig. 7. For comparison,
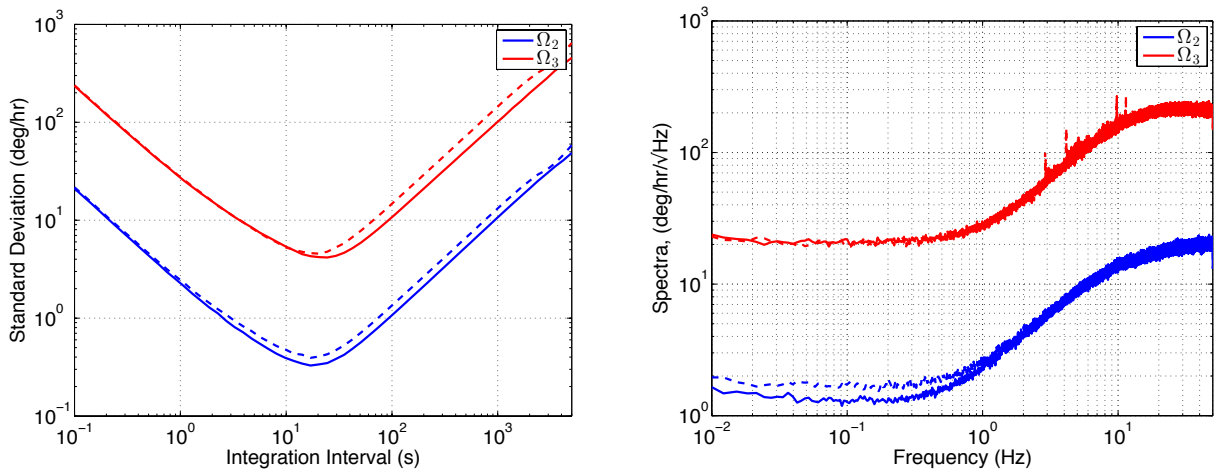

Fig. 5. Left: Allan deviation of Ω_2 and Ω_3. Right: PSD of Ω_2 and Ω_3. The solid lines are obtained from tests where the two mode pairs are operated separately and independently. The dash lines are from simultaneous dual mode operation. Figures from [9].
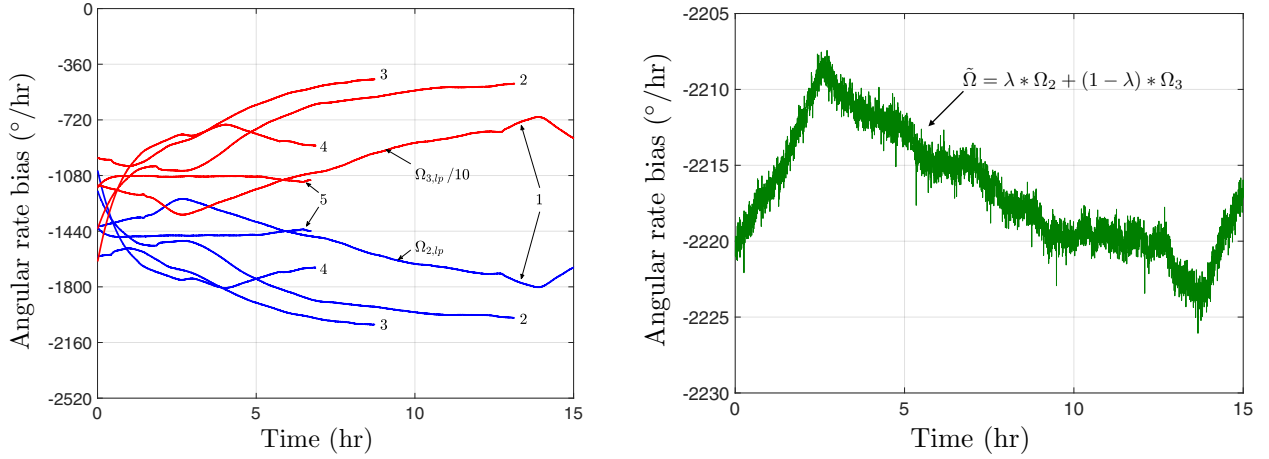
Fig. 6. Left: low-pass filtered signals $\Omega_{2,lp}$ (blue, solid) and $\Omega_{3,lp}/10$ (red) from five dual-pair experiments (labeled "1" through "5") exhibit strong correlation within a given experiment. Right: the fused rate $\tilde{\Omega}_{lp} = \lambda\Omega_{2,lp} + (1-\lambda)\Omega_{3,lp}$ (green) from experiment 1, where $\lambda = 0.9192$.
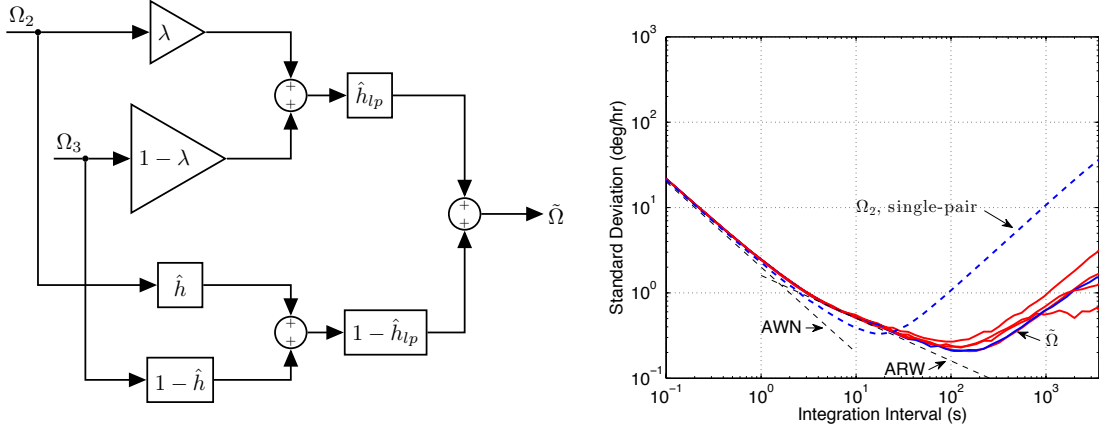

Fig. 7. Left: block diagram showing the complementary filter structure for fusing Ω_2 and Ω_3 into a single signal. Right: Allan deviation of fused rate $\tilde{\Omega}$ across the 5 data runs shown in Fig. 6. The solid blue trace was used to fit the filters for the fusion of Ω_2 and Ω_3 into $\tilde{\Omega}$. For comparison, the blue dash is the Allan deviation for Ω_2 from an experiment using only the $n = 2$ modes. The angle white noise (AWN) and angle random walk (ARW) asymptotes for $\tilde{\Omega}$ are also shown. Figures from [9].

the Allan deviation of a rate measurement using only the $n = 2$ mode pair is plotted in the same figure (dash blue line). There is significant improvement in long-term bias stability with short-term noise essentially equal to that of $n = 2$ rate. In fact, the stability of $\tilde{\Omega}$ has improved to the point where the ARW trend is readily identifiable in the Allan deviation, whereas it is obscured in the single-pair Allan deviation by the onset of rate ramping. The fused rate signal has an ARW figure of $0.027°/\sqrt{\text{hr}}$. The angle white noise (AWN) asymptote is also shown in Fig. 7. Another significance is that the fused rate measurement provided effective mitigation to rate ramping. In the case involving only $n = 2$ modes, rate ramping occurs roughly at 20-second integration time. In contrast, the fused rate experience no rate ramping until after 200 seconds of integration time, and offers about 20 times reduction in long term instability.

C. Temperature sensitivity reduction

The bias drift correlation is particularly effective for reducing temperature induced bias drifts. To demonstrate its effectiveness, a set of thermal cycle tests were conducted. In each test a periodic thermal disturbance was introduced by a heater-RTD chip attached beneath the MEMS resonator. The thermal profile is given by the plot on the left side in Fig. 8. The induced bias drifts over the test period are plotted on the right. It is evident that there is very strong correlation between the $n = 2$ and $n = 3$ bias drifts. The complementary filter is applied to the rate measurements using the same correlation constant. It is remarkable to notice that the fused rate measurement using the correlation achieves a bias temperature sensitivity reduction of over 500 times! It is also worthwhile to point out that the same test was repeated several times over a period of 6 months, and the correlation constant stayed virtually unchanged. Table II compares the temperature sensitivities of different modes of measurement.
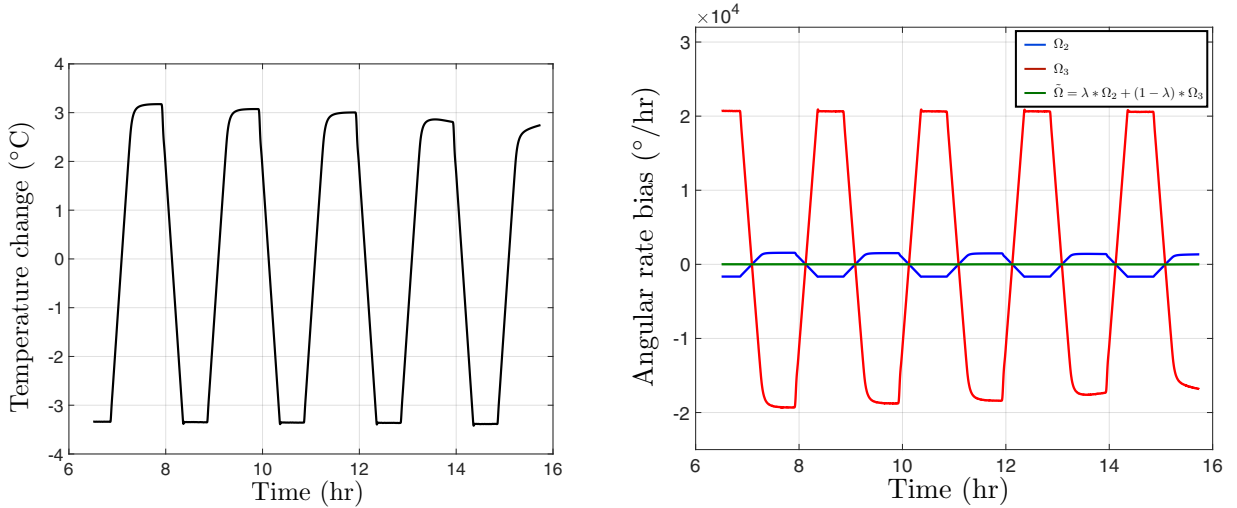
Fig. 8. Left: Temperature disturbance driven by a heater-RTD chip attached beneath the resonator. The temperature on the ordinate is the deviation from the nominal operating temperature. Right: Comparison of temperature induced bias drift between $n = 2$ and $n = 3$ modes. The fused rate measurement using the complementary filter structure shown in Fig. 7 achieves a reduction in temperature sensitivity by a factor of 500.

TABLE II
BIAS TEMPERATURE SENSITIVITIES AND CORRELATION BETWEEN THE $n = 2$ AND $n = 3$ MODE

Measurement Mode	Bias Temperature Sensitivity ($^\circ$/hr/$^\circ$C)
$n = 2$ mode	482
$n = 3$ mode	-6134
Fused measurement	0.95

D. Vacuum Pressure Sensitivity Mitigation

The resonator is not vacuum sealed at the device level and so allows us to study the impact of vacuum pressure drift on gyro bias. The result could offer some insight into pressure-induced bias drift in a vacuum packaged device, where material outgassing and molecular diffusion would lead to gradual vacuum degradation over the device life. To avoid conflation with temperature induced drift, the heater-RTD chip described in the previous section is utilize in this test to maintain constant resonator temperature. Peak-to-peak temperature variation throughout the test is maintained to within $10 \, \text{m}^\circ$C. The test is started with a chamber pressure of $27 \, \mu$Torr, and over the course of five hours, the turbo pump reduces the chamber pressure while the $n = 2$ and $n = 3$ pairs are simultaneously operating as CVGs. The chamber pressure is recorded by a cold cathode pressure gauge, and is plotted on the left in Fig. 9. Gyro bias from both the $n = 2$ and $n = 3$ modes are simultaneously recorded over the test period in a zero rate environment. The drift induced by pressure on Ω_2 is 2.6°/hr/μTorr. Using the same proportionality constant found in the previous section, the fused rate measurement $\tilde{\Omega}$ shows remarkable rejection to this vacuum disturbance. A linear fit over the residual estimates the vacuum pressure sensitivity is reduced to less than 0.05°/hr/μTorr, and is completely uncorrelated to the pressure drift. Ω_2 and $\tilde{\Omega}$ are plotted on the right in Fig. 9.

IV. CONCLUSION

A technique has been developed to simultaneously operate the $n = 2$ and $n = 3$ pairs of Coriolis-coupled modes in a single resonator. The angular rate extracted from the $n = 2$ pair is compared to that of the $n = 3$ pair. The rate biases of the two mode pairs exhibit strong correlation over longer intervals, thus, a complementary filter structure is proposed to fuse the two rate measurements into a single rate estimate with improved long-term stability and low short-term noise. The correlation between the two modes has also been shown to be very constant over temperature excursion and extended periods of time. Tests show the fused rate measurements offer temperature sensitivity reduction of over 500 times, and almost complete rejection of vacuum disturbance over the limited test range.

REFERENCES

[1] S. Zotov, A. Trusov, and A. Shkel, "Three-dimensional spherical shell resonator gyroscope fabricated using wafer-scale glassblowing," *IEEE J. Microelectromech. Syst.*, vol. 21, no. 3, pp. 509 – 510, June 2012.

[2] J. Y. Cho, J.-K. Woo, J. Yan, R. Peterson, and K. Najafi, "Fused-silica micro birdbath resonator gyroscope (μ-BRG)," *IEEE J. Microelectromech. Syst.*, vol. 23, no. 1, pp. 66 – 77, Feb 2014.
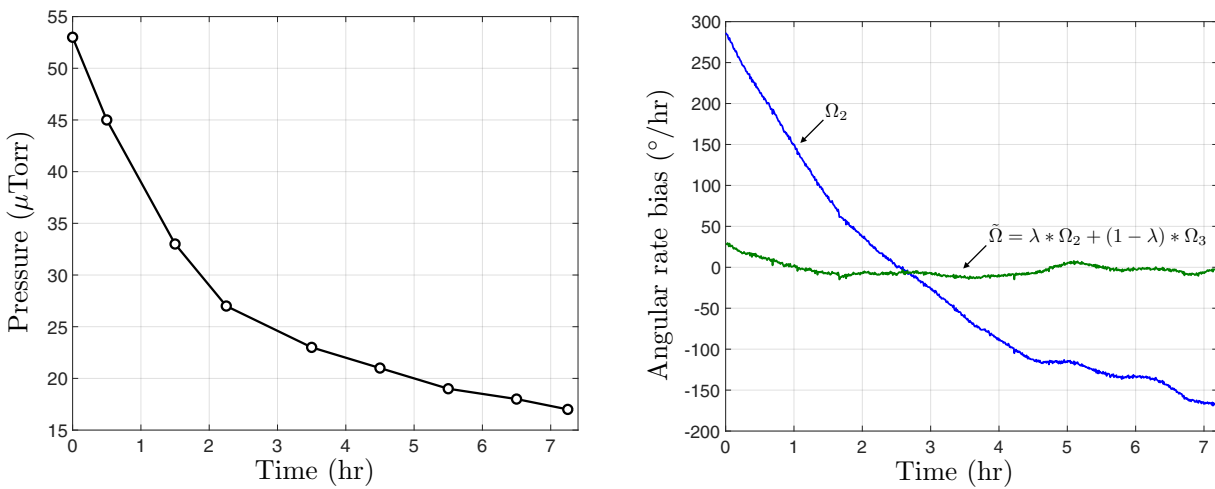
Fig. 9. Left: vacuum chamber pressure vs. time, recorded by a cold cathode gauge. Right: vacuum pressure induced bias drift over time. Peak bias drift over the test period is 454.5^0/hr for Ω_2, with an estimated sensitivity of 12.6 $^o/hr/\mu$Torr. The rused rate measurement (using $\lambda = 0.9192$) shows almost complete rejection of vacuum disturbance. A linear fit of the residual error indicates sensitivity is reduced to about 0.25 $^o/hr/\mu$Torr.

[3] P. Taheri-Tehrani, T.-H. Su, A. Heidari, G. Jaramillo, C. Yang, S. Akhbari, H. Najar, S. Nitzan, D. Saito, L. Lin, and D. Horsley, "Micro-scale diamond hemispherical resonator gyroscope," in *Proc. Solid-State Sensors, Actuators and Microsystems Workshop*, Hilton Head, SC, June 2014, pp. 289 – 292.

[4] I. Prikhodko, S. Zotov, A. Trusov, and A. Shkel, "Foucault pendulum on a chip: Rate integrating silicon mems gyroscope," *Sensors and Actuators A: Physical*, vol. 177, pp. 67 – 78, April 2012.

[5] Y. Yang, E. J. Ng, Y. Chen, I. B. Flader, and T. W. Kenny, "A unified epi-seal process for fabrication of high-stability microelectromechanical devices," *JMEMS*, vol. 25, no. 3, pp. 489 – 497, June 2016.

[6] P. Shao, C. Mayberry, X. Gao, V. Tavassoli, and F. Ayazi, "A polysilicon microhemispherical resonating gyroscope," *J. Microelectromech. Syst.*, vol. 23, pp. 762–764, Aug 2014.

[7] A. Challoner, H. Ge, and J. Liu, "Boeing disc resonator gyroscope," in *Proc. 2014 IEEE/ION Position, Location and Navigation Symp.*, Monterey, CA, May 2014, pp. 504–514.

[8] A. Efimovskaya, D. Wang, Y.-W. Lin, and A. M. Shkel, "On ordering of fundamental wineglass modes in toroidal ring gyroscope," in *Sensors*, Feb 2016, pp. 1–3.

[9] H. Ge and R. MCloskey, "Simultaneous angular rate estimates extracted from a single axisymmetric resonator," *IEEE Sensors Journal*, vol. 17, no. 22, pp. 7460–7469, Nov 2017.

[10] H. H. Ge, D. Kim, and R. Mcloskey, "Simultaneous exploitation of the fundamental and higher order wineglass modes in a vibratory gyro," in *2015 IEEE International Symposium on Inertial Sensors and Systems (ISISS) Proceedings*, March 2015, pp. 1–4.

[11] D. Kim and R. M'Closkey, "A systematic method for tuning the dynamics of electrostatically actuated vibratory gyros," *IEEE Trans. Control Syst. Technol.*, vol. 14, pp. 69–81, Jan. 2006.

[12] A. H. Behbahani and R. T. M'Closkey, "Frequency analysis of a uniform ring perturbed by point masses and springs," *Journal of Sound and Vibration*, vol. 397, pp. 204 – 221, June 2017.

[13] A. H. Behbahani, D. Kim, P. Stupar, J. DeNatale, and R. T. M'Closkey, "Tailored etch profiles for wafer-level frequency tuning of axisymmetric resonators," *Journal of Microelectromechanical Systems*, 2017.

[14] Y. Yang, E. J. Ng, Y. Chen, I. B. Flader, and T. W. Kenny, "Mode-matching of wineglass mode disk resonator gyroscope in (100) single crystal silicon," *JMEMS*, vol. 24, no. 2, pp. 343–350, April 2015.